Article
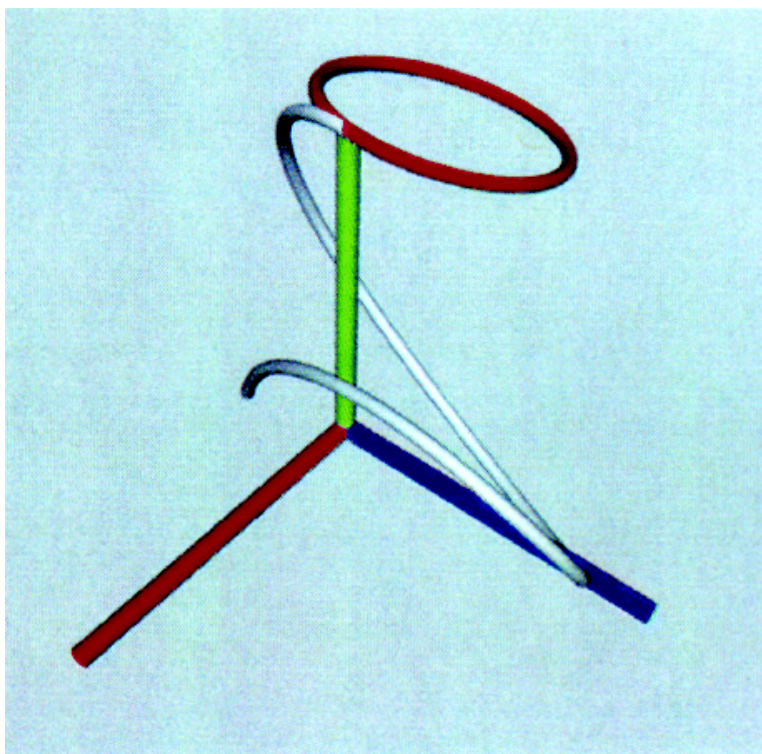
A Study of Homonuclear Dipolar Recoupling Pulse Sequences in Solid-State Nuclear Magnetic Resonance

T. Karlsson, J. M. Popham, J. R. Long, N. Oyler, and G. P. Drobny

More About This Article

Additional resources and features associated with this article are available within the HTML version:

- Supporting Information
- Links to the 3 articles that cite this article, as of the time of this article download
- Access to high resolution figures
- Links to articles and content related to this article
- Copyright permission to reproduce figures and/or text from this article

J|A|C|S

A R T I C L E S

A Study of Homonuclear Dipolar Recoupling Pulse Sequences in Solid-State Nuclear Magnetic Resonance

T. Karlsson,[†] J. M. Popham,[†] J. R. Long,[#] N. Oyler,[▽] and G. P. Drobny*,[†]

Contribution from the Department of Chemistry, University of Washington, Seattle, Washington 98195, Department of Biochemistry and Molecular Biology, University of Florida, Gainesville, Florida 32611, and Laboratory of Chemical Physics, NIDDK, National Institutes of Health, Bethesda, Maryland 20892

Received November 21, 2002; E-mail: drobny@chem.washington.edu

Abstract: Dipolar recoupling pulse sequences are of great importance in magic angle spinning solid-state NMR. Recoupling sequences are used for excitation of double-quantum coherence, which, in turn, is employed in experiments to estimate internuclear distances and molecular torsion angles. Much effort is spent on the design of recoupling sequences that are able to produce double-quantum coherence with high efficiency in demanding spin systems, i.e., spin systems with small dipole−dipole couplings and large chemical-shift anisotropies (CSAs). The sequence should perform robustly under a variety of experimental conditions. This paper presents experiments and computer calculations that extend the theory of double-quantum coherence preparation from the strong coupling/small CSA limit to the weak coupling limit. The performance of several popular dipole−dipole recoupling sequences—DRAWS, POST-C7, SPC-5, R14$_2^6$, and R22$_4^9$—are compared. It is found that the optimum performance for several of these sequences, in the weak coupling/large CSA limit, varies dramatically, with respect to the sample spinning speed, the magnitude and orientation of the CSAs, and the magnitude of dipole−dipole couplings. It is found that the efficiency of double-quantum coherence preparation by γ-encoded sequences departs from the predictions of first-order theory. The discussion is supported by density-matrix calculations.

1. Introduction

Nuclear magnetic resonance (NMR) is a sophisticated tool for the investigation of matter on an atomic and molecular level. NMR is used to estimate the molecular geometry of many different phases of matter, e.g., liquids, liquid crystals, polymers, and polycrystalline solids. NMR is also established as a successful tool to estimate molecular dynamics on a wide range of time scales.

In solids, high-resolution NMR spectra are generally obtained while spinning the sample rapidly about the angle $\theta = \tan^{-1}(\sqrt{2})$, with respect to an external static magnetic field B_0. This is called magic angle spinning (MAS).[1,2] To enhance the spectral sensitivity of rare, low-gamma nuclei, MAS is combined with cross polarization (CP) from abundant protons.[3]

To first order, MAS suppresses the effect of anisotropic spin interactions, such as chemical-shift anisotropies (CSAs) and direct dipole−dipole couplings. If the sample rotation speed is slower than the magnitude of the anisotropy of the interaction, a set of equally spaced peaks,[4] called spinning sidebands, are observed in the spectrum. The spacing between each pair of peaks is equal to the sample rotation speed, whereas the

frequency spacing between the left- and right-most sidebands, as well as the individual sideband amplitudes, are functions of the CSA interaction. If the spinning frequency is larger than the anisotropy of the interaction, only one peak at the isotropic value is observed.

The suppression of spin interactions under MAS seems unfortunate, because anisotropic information about the chemical environment and the molecular geometry is lost. Much effort is therefore spent to reintroduce nuclear spin interactions in a controlled fashion under MAS. In this context, the dipole−dipole coupling is of particular interest, because it represents a direct estimate of molecular geometry through its dependence on the internuclear distance, r, between involved nuclei. An active dipole−dipole coupling may also be used for the excitation of double-quantum coherence. Double-quantum coherence experiments allow for effective suppression of unwanted signals arising from natural abundant nuclei, while leaving signals arising from coupled spin pairs.

Several techniques to estimate internuclear distances[5−12] and molecular torsion angles[13−19] make use of double-quantum

[†] University of Washington.
[#] University of Florida.
[▽] National Institutes of Health.
(1) Lowe, I. J. *Phys. Rev. Lett.* **1959**, *2*, 285.
(2) Andrew, E. R.; Bradbury, A.; Eades, R. G. *Nature* **1959**, *183*, 1802.
(3) Pines, A.; Gibby, M. G.; Waugh, J. S. *J. Chem. Phys.* **1972**, *56*, 1776.
(4) Maricq, M. M.; Waugh, J. S. *J. Chem. Phys.* **1979**, *70*, 3300.

(5) Creuzet, F.; McDermott, A.; Gebhard, R.; van der Hoef, K.; Spijker-Assink, M. B.; Herzfeld, J.; Lugtenburg, J.; Levitt, M. H.; Griffin, R. G. *Science* **1991**, *251*, 783.
(6) Peersen, O. B.; Yoshimura, S.; Hojo, H.; Aimoto, S.; Smith, S. O. *J. Am. Chem. Soc.* **1992**, *114*, 4332.
(7) Studelska, D. R.; Klug, C. A.; Beusen, D. D.; McDowell, L. M.; Schaefer, J. *J. Am. Chem. Soc.* **1996**, *118*, 5476.
(8) Verdegem, P. J. E.; Helmle, M.; Lugtenburg, J.; de Groot, H. J. M. *J. Am. Chem. Soc.* **1997**, *119*, 169.

coherence. In some cases, experiments may also utilize the CSA interaction in combination with double-quantum coherence to estimate molecular geometry.[20−22] In the following discussion, we note that most techniques designed for high-accuracy measurement of internuclear distances through the dipole−dipole coupling require samples containing isolated, isotopically labeled pairs of spins, e.g., ^{13}C−^{13}C pairs.

Important features of any double-quantum coherence excitation technique are the *excitation efficiency* of double-quantum coherence and the time scale on which the excitation occurs. Low double-quantum excitation efficiency (ϵ^{DQ}) results in low sensitivity of spectral peaks, leading to time-consuming experiments. Slow excitation of double-quantum coherence, on the other hand, causes relaxation processes to dominate, leading to a quenching of the resulting signal. Therefore, much effort is spent on the design of recoupling sequences that are able to produce double-quantum coherence with high efficiency and on a short time scale.

Generally, the recoupling efficiency in a polycrystalline powder is a function of crystallite orientation. In a powder, all possible crystallite orientations exist and the total recoupling efficiency is an average over these orientations. For a particular crystallite, a set of Euler angles, $\Omega^{CR} = (\alpha^{CR}, \beta^{CR}, \gamma^{CR})$, defines the crystallite's orientation, with respect to a globally defined frame (e.g., a frame fixed at the sample rotor). Two classes of recoupling sequences may be identified. In the first class, the recoupling efficiency depends on the Euler angles β^{CR} and γ^{CR}, and in the second class, the efficiency only depends on β^{CR}. These classes are called γ-dependent and γ-independent sequences, respectively. If the CSA is present, the recoupling also depends on the Euler angle α^{CR} for both the γ-dependent and the γ-independent type of recoupling sequences.

The recoupling sequences DRAMA,[23,24] MELODRAMA,[25] and DRAWS[10,11] are all dependent on γ. The theoretical double-quantum excitation efficiency for this class of pulse sequences is ∼52%.[26]

HORROR,[26] C7,[27] POST-C7,[28] SPC-5,[29] and the family of R-sequences[30] are γ-independent recoupling sequences. To first order, γ-independent pulse sequences show a higher theoretical double-quantum coherence excitation efficiency ($\epsilon^{DQ} \approx 73\%$).[26]

Even though the theoretical efficiency of the γ-independent sequences is higher, the choice of one recoupling sequence in favor of another is not obvious. Several factors determine the excitation efficiency in practice: (i) the magnitude of the homonuclear dipole−dipole coupling constant; (ii) CSA interactions; (iii) heteronuclear interactions; and (iv) experimental factors, such as radio-frequency (rf) inhomogeneity and rf phase transients.

The magnitude of the homonuclear dipole−dipole coupling constant constitutes the largest constraint on the final excitation efficiency. The dipole−dipole constant, b_{jk} (rad s^{-1}), between two chemical sites j and k, is given by

$$b_{jk} = -\left(\frac{\mu_0}{4\pi}\right)\frac{\gamma_j\gamma_k\hbar}{r_{jk}^3} \tag{1}$$

where μ_0 and $\hbar$ are constants; γ_j and γ_k are the gyromagnetic ratio of each respective nucleus, and r_{jk} is the internuclear distance between spins j and k. Equation 1 indicates that, as the internuclear distance increases, the dipole−dipole coupling constant decreases. In practice, a decreasing coupling constant implies an increasing excitation time. At long excitation times, relaxation effects dominate the spin dynamics, which effectively quench any coherence and therefore constitute the main constraints in this type of experiment. Dephasing due to relaxation obscures dephasing due to the dipole−dipole coupling, leading to poor estimates of the internuclear distance.[31]

The CSA interaction, on the other hand, is addressed by designing a sequence that suppresses the interaction internally. The magnitude of the CSA interaction is proportional to the static magnetic field B_0; therefore, in some circumstances, it may be beneficial to perform the experiment at low magnetic fields, particularly if the CSAs are very large. In this paper, we observe that, for a fixed dipole−dipole coupling constant, the magnitude of the CSA interaction is the main factor that differentiates different recoupling sequences in terms of the recoupling efficiency.

Heteronuclear interactions, such as couplings between observed nuclei and abundant protons, are suppressed with different spin-decoupling techniques. The most common method is to apply a strong, continuous rf field at the proton frequency, i.e., continuous-wave (CW) decoupling.[3,32] Other techniques, such as TPPM[33] or CN$_n^\nu$ sequences,[34] may also be used. It is found, however, that these techniques most often are not fully capable of suppressing strong heteronuclear couplings and may also perform with different efficiencies, depending on the actual rf sequence applied to the other channels.

Poor rf coil design results in the problem of rf inhomogeneity. Sufficient rf homogeneity is usually achieved by confining the sample to a small volume in the sample rotor, where the applied

 (9) Feng, X.; Verdegem, P. J. E.; Lee, Y. K.; Helmle, M.; Shekar, S. C.; de Groot, H. J. M.; Lugtenburg, J.; Levitt, M. H. *Solid State NMR* **1999**, *14*, 81.
(10) Mehta, M. A.; Gregory, D. M.; Kiihne, S.; Mitchell, D. J.; Hatcher, M. E.; Shiels, J. C.; Drobny, G. P. *Solid State NMR* **1996**, *7*, 211.
(11) Gregory, D. M.; Mehta, M. A.; Shiels, J. C.; Drobny, G. P. *J. Chem. Phys.* **1997**, *107*, 28.
(12) McDermott, A. E.; Creuzet, F.; Gebhard, R.; van der Hoef, K.; Levitt, M. H.; Herzfeld, J.; Lugtenburg, J.; Griffin, R. G. *Biochemistry* **1994**, *33*, 6129.
(13) Schmidt-Rohr, K. *J. Am. Chem. Soc.* **1996**, *118*, 7601.
(14) Feng, X.; Lee, Y. K.; Sandström, D.; Edén, M.; Maisel, H.; Sebald, A.; Levitt, M. H. *Chem. Phys. Lett.* **1996**, *257*, 314.
(15) Feng, X.; Edén, M.; Brinkmann, A.; Luthman, H.; Eriksson, L.; Gräslund, A.; Antzutkin, O. N.; Levitt, M. H. *J. Am. Chem. Soc.* **1997**, *119*, 12006.
(16) Feng, X.; Verdegem, P. J. E.; Lee, Y. K.; Sandström, D.; Edén, M.; Bovee-Geurts, P.; de Grip, W. J.; Lugtenburg, J.; de Groot, H. J. M.; Levitt, M. H. *J. Am. Chem. Soc.* **1997**, *119*, 6853.
(17) Hong, M.; Gross, J. D.; Griffin, R. G. *J. Phys. Chem. B* **1997**, *101*, 5869.
(18) Costa, P. R.; Gross, J. D.; Hong, M.; Griffin, R. G. *Chem. Phys. Lett.* **1997**, *280*, 95.
(19) Ishii, Y.; Terao, T.; Kainosho, M. *Chem. Phys. Lett.* **1996**, *256*, 133.
(20) Weliky, D. P.; Tycko, R. *J. Am. Chem. Soc.* **1996**, *118*, 8487.
(21) Tycko, R.; Weliky, D. P.; Berger, A. E. *J. Chem. Phys.* **1996**, *105*, 7915.
(22) Bower, P. V.; Oyler, N.; Mehta, M. A.; Long, J. R.; Stayton, P. S.; Drobny, G. P. *J. Am. Chem. Soc.* **1999**, *121*, 8373.
(23) Tycko, R.; Dabbagh, G. *Chem. Phys. Lett.* **1990**, *173*, 461.
(24) Tycko, R.; Dabbagh, G. *J. Am. Chem. Soc.* **1991**, *113*, 9444.
(25) Sun, B. Q.; Costa, P. R.; Kociso, D.; Lansburgy, P. T.; Griffin, R. G. *J. Chem. Phys.* **1995**, *102*, 702.
(26) Nielsen, N. C.; Bildsøe, H.; Jakobsen, H. J.; Levitt, M. H. *J. Chem. Phys.* **1994**, *101*, 1805.
(27) Lee, Y. K.; Kurur, N. D.; Helmle, M.; Johannessen, O. G.; Nielsen, N. C.; Levitt, M. H. *Chem. Phys. Lett.* **1995**, *242*, 304.
(28) Hohwy, M.; Jakobsen, H. J.; Edén, M.; Levitt, M. H.; Nielsen, N. C. *J. Chem. Phys.* **1998**, *108*, 2686.
(29) Hohwy, M.; Rienstra, C. M.; Jaroniec, C. P.; Griffin, R. G. *J. Chem. Phys.* **1999**, *110*, 7983.
(30) Brinkmann, A.; Levitt, M. H. *J. Chem. Phys.* **2001**, *115*, 357.
(31) Karlsson, T.; Brinkmann, A.; Verdegem, P. J. E.; Lugtenburg, J.; Levitt, M. H. *Solid State NMR* **1999**, *14*, 43.
(32) Schaefer, J.; Stejskal, E. O. *J. Am. Chem. Soc.* **1976**, *98*, 1031.
(33) Bennett, A. E.; Rienstra, C. M.; Auger, M.; Lakshmi, K. V.; Griffin, R. G. *J. Chem. Phys.* **1995**, *103*, 6951.
(34) Edén, M.; Levitt, M. H. *J. Chem. Phys.* **1999**, *111*, 1511.
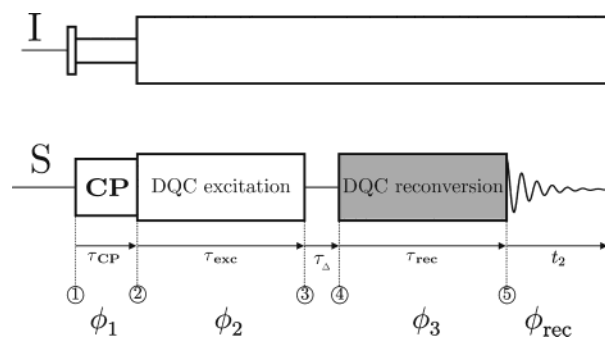
Figure 1. Generalized rf pulse sequence for excitation of double-quantum coherence. The top row shows rf fields applied on *I*-spins (e.g., ^{1}H-spins), and the bottom row denotes rf fields applied on the *S*-spins (e.g., ^{13}C, ^{15}N). See text for details.

rf field can be assumed to be homogeneous. The condition of rf inhomogeneity may also arise as an intrinsic property of the sample itself. Phase transients, on the other hand, occur when the spectrometer rf phase is switching from one value to another. If the duration of such transients is long, compared to the actual rf pulse length, the efficiency of the pulse sequence may be degraded. Exactly how these experimental factors affect the performance of a certain pulse sequence is not examined in this work.

This paper focuses on the performance of different recoupling techniques as a function of the magnitude of the CSA, dipole−dipole interactions, and sample rotation speed. We have restricted the study to what we believe are the most widely used and optimized sequences, and several other homonuclear recoupling techniques have therefore been left out of the discussion. For example, rotational resonance,[35,36] one of the most successful methods for estimating internuclear distances, may be used for efficient excitation of double-quantum coherence,[37,38] with a short excitation time. Rotational resonance dipolar recoupling is caused by the sample rotation itself, rather than being introduced by external rf intervention; therefore, rotational resonance is not discussed in this paper.

In this paper, we are studying five different rf dipolar recoupling pulse sequences: DRAWS, POST-C7, SPC-5, R14$_2^6$, and R22$_4^9$. The study is based on numerical density-matrix calculations, using the SIMPSON[39] and Gullringen[40] programs. Experiments on a wide range of samples are presented to support and emphasize the theoretical findings.

2. Dipolar Recoupling Sequences

Figure 1 is a symbolic description of a rf pulse sequence suitable for excitation of double-quantum coherence in an organic, polycrystalline solid under MAS. The top row shows the rf irradiation applied on the *I*-spins (usually protons, ^{1}H), and the bottom row denotes the rf fields applied to the *S*-spins (e.g., ^{13}C or ^{15}N). The circled numbers, ①−⑤, denote specific time points within the pulse sequence.

(35) Andrew, E. R.; Bradbury, A.; Eades, R. G.; Wynn, V. T. *Phys. Lett.* **1963**, *4*, 99.
(36) Raleigh, D. P.; Levitt, M. H.; Griffin, R. G. *Chem. Phys. Lett.* **1988**, *146*, 71.
(37) Karlsson, T.; Edén, M.; Luthman, H.; Levitt, M. H. *J. Magn. Reson.* **2000**, *145*, 95.
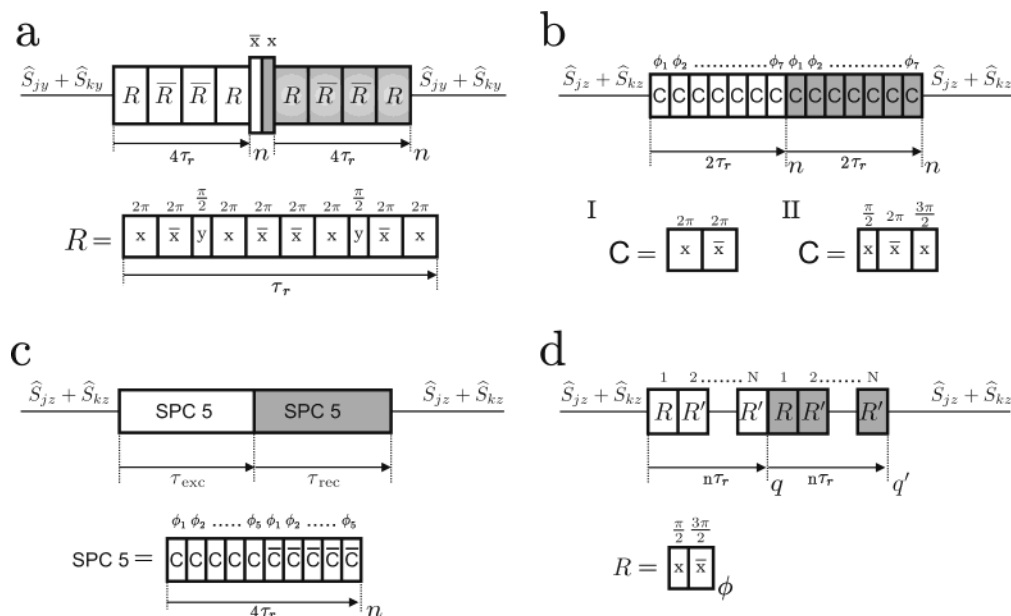(38) Karlsson, T.; Hughes, C. E.; auf der Günne, J. S.; Levitt, M. H. *J. Magn. Reson.* **2001**, *148*, 238.
(39) Bak, M.; Rasmussen, J. T.; Nielsen, N. C. *J. Magn. Reson.* **2000**, *147*, 296.
(40) Karlsson, T.; Drobny, G. P., manuscript in preparation, 2002.

The pulse sequence starts with a cross-polarization sequence,[3] whose purpose is to transfer magnetization from the abundant *I*-spins to the *S*-spins. In the *I*-spin channel, cross polarization is initiated by a strong $\pi/2$-pulse, creating transverse ^{1}H magnetization. The ^{1}H magnetization is subsequently spin-locked by an rf field applied over a time of length τ_{CP}, between timepoints ① and ② in Figure 1. During τ_{CP}, the rf-field strengths of the *I*- and *S*-spins are matched to satisfy the Hartmann−Hahn condition,[41] allowing *I*-spin polarization to be transferred to the *S*-spins. For the rest of the sequence, a strong rf field is applied to the *I*-spin channel, whose purpose is to decouple the *I*-spins from the *S*-spins.[3] To achieve a more stable and reproducible transfer of *I*-spin polarization,[42] it is common practice, especially at high sample rotation frequencies, to ramp the rf field on either the *I*- or *S*-spins, during the cross-polarization step.

In the *S*-spin channel, a block denoted as DQC (double-quantum coherence) excitation follows after the cross-polarization block. The time duration of this block is denoted τ_{exc}. The purpose of this block is to excite double-quantum coherence. The inner working of this block is different for different recoupling sequences and is discussed in more detail for individual sequences below.

The DQC excitation block is followed by a time interval of length τ_Δ, between timepoints ③ and ④, allowing for free precession of the double-quantum coherence. In experiments where the evolution of double-quantum coherence is exploited, this interval is incremented. For experiments where the evolution of double-quantum coherence is unimportant, this interval is kept constant or is completely removed.

The block between timepoints ④ and ⑤, with a time duration of τ_{rec}, converts double-quantum coherence to single-quantum coherence, i.e., observable magnetization. The block is shaded, indicating that a double-quantum coherence filter is applied. The double-quantum filter selects the signal from spins participating in a developed double-quantum coherence state at timepoint ④, thus filtering out coherence signals from any isolated spins.

To select a desired coherence transfer pathway (CTP), specific cycling of phases for each rf block, with respect to the receiver, is applied. In Figure 1, the overall phase of each individual pulse sequence block is denoted as $\phi_1...\phi_3$. The rf receiver phase is denoted as ϕ_{rec}. These phases are cycled between different acquired transients, to select signals from the desired CTP. The phases of the pulse sequence blocks, $\phi_1...\phi_3$, generally may be cycled according to

$$\phi_1 = \frac{2\pi m}{n_1} + \phi_1^0 \qquad (2)$$

$$\phi_p = \frac{2\pi}{n_p}\text{floor}\left(\frac{m}{n_1 n_2 ... n_{p-1}}\right) + \phi_p^0 \qquad \text{(for } p > 1) \qquad (3)$$

where the function floor(*x*) returns the largest integer not greater than *x*. Here, ϕ_p^0 is the initial phase of the pulse sequence block ϕ_p and *m* is the transient counter *m* ($m = 0, 1, 2, ..., n_{tot} - 1$, where n_{tot} is the total number of transients in a complete phase cycle, $n_1 n_2 n_3 n_{rec}$). A suitable choice for selecting a transfer of double-quantum coherence at timepoint ④ to single-quantum

(41) Hartmann, S. R.; Hahn, E. L. *Phys. Rev.* **1962**, *128*, 2042.
(42) Metz, G.; Wu, X.; Smith, S. O. *J. Magn. Reson., Ser. A* **1994**, *110*, 219.

Figure 2. Figure showing different dipole−dipole recoupling sequences: (a) DRAWS, (b) C7 and POST-C7 (panels I and II, respectively), (c) SPC-5, and (d) the R family of sequences.

Table 1. Specific Cycling of Phases for Each rf Block ($\phi_1...\phi_3$) in Figure 1, with Respect to the Receiver Phase (ϕ_{rec})

transient counter, m	angle (deg)[a]			
	ϕ_1	ϕ_2	ϕ_3	ϕ_{rec} (deg)
0	0	0	0	0
1	0	0	90	270
2	0	0	180	180
3	0	0	270	90

[a] $\phi_1...\phi_3$ is the overall phase of each individual pulse-sequence block. This phase cycle selects a coherence transfer of order $\pm 2 \rightarrow -1$ between timepoints ④ and ⑤ in Figure 1.

coherence, at timepoint ⑤, is $n_1 = 1$, $n_2 = 1$, $n_3 = 4$, $n_{tot} = 4$. On each transient, the receiver phase is adjusted to satisfy the equation

$$1(\phi_1 - \phi_1^0) + 1(\phi_2 - \phi_2^0) - 3(\phi_3 - \phi_3^0) + \phi_{rec} = 0 \quad (4)$$

This phase cycle selects a coherence transfer of the order $\pm 2 \rightarrow -1$ between timepoints ④ and ⑤ in Figure 1. The actual phases for each pulse sequence block at a certain transient are tabulated in Table 1.

Specific dipole−dipole rf-recoupling sequences are shown in Figure 2a−d. The sequences are DRAWS (Figure 2a), C7 and POST-C7 (Figure 2b, panels I and II, respectively), SPC-5 (Figure 2c), and the family of R sequences (Figure 2d). For simplicity, the cross-polarization step and the proton spin decoupling sequence have been left out of these figures. A brief discussion of each of the recoupling sequences is given below.

2.1. DRAWS. Figure 2a shows the DRAWS[11] dipole−dipole recoupling sequence, in the context of double-quantum coherence excitation. It is assumed that the sequence is taking advantage of cross polarization and proton spin decoupling, as shown in Figure 1. It is also assumed that the cross-polarization sequence shown in Figure 1 creates transverse magnetization along the y-axis in the rotating frame, corresponding to an initial density operator proportional to $(\hat{S}_{jy} + \hat{S}_{ky})$, as indicated in the figure.

In Figure 2a, four R and $\bar{R}$ elements occupy four rotor periods, $4 \times \tau_r$; the pulses comprising a single R element are shown below the top row. The $\bar{R}$ element is a phase-shifted R element, obtained by adding π to each internal phase for each pulse in the R element. Each R element is composed of 10 rf pulses, with different phases and flip angles, and occupies one rotational period, τ_r. In Figure 2a, wide rectangles correspond to pulses with flip angles of 2π and narrow rectangles correspond to pulses with flip angles of $\pi/2$. The rf amplitude of each pulse is chosen such that the S-spin nutation frequency satisfies the condition $\omega_{rf}^S = 8.5 \times \omega_r$ throughout the sequence.

For efficient excitation of double-quantum coherence, four R and $\bar{R}$ elements are supercycled as $R\bar{R}\bar{R}R$. Such a supercycle greatly improves the overall performance of the sequence, by suppressing effects due to the CSA interaction. The supercycle is generally repeated n times, i.e., $\tau_{exc} = n \times (4\tau_r)$, and double-quantum coherence is excited by a strong $\pi/2$-pulse, corresponding to timepoint ③ in Figure 1. It should be noted that the sampling interval can be made shorter by sampling between the R elements.

Reconversion of double-quantum coherence into observable single-quantum coherence is initiated by another strong $\pi/2$-pulse, followed by n repetitions of the $R\bar{R}\bar{R}R$ block. In Figure 2a, the second part of the sequence is shaded, indicating a conventional double-quantum coherence filter, as discussed previously.

2.2. C7 and POST-C7. Both the C7[27] and POST-C7[28] pulse sequences are shown in Figure 2b, in panels I and II, respectively. It is assumed that longitudinal magnetization is prepared, i.e., $(\hat{S}_{jz} + \hat{S}_{kz})$, prior to application of the sequence. This is achieved by inserting a single $\pi/2$-pulse after the initial cross-polarization sequence shown in Figure 1.

Both C7 and POST-C7 consist of a sequence of seven rf cycles C, occupying two rotational periods, $2 \times \tau_r$. The overall phase of each consecutive cycle, ϕ, is incremented in steps of $2\pi/7$. The rf amplitude throughout the sequence is set to satisfy the condition $\omega_{rf}^S = 7 \times \omega_r$.

The difference between C7 and POST-C7 is the inner construction of the rf cycle C, as shown in panels I and II in Figure 2b. The original C7 cycle consists of two rf pulses, each with a flip angle 2π, and phases x and $\bar{x}$, respectively. The POST-C7 cycle, on the other hand, is constructed from three rf pulses, with three flip angles $\{\pi/2, 2\pi, 3\pi/2\}$ and rf phases $\{x, \bar{x}, x\}$. It has been shown that the POST-C7 cycle has superior performance, compared to the original C7 cycle.[28]

To excite double-quantum coherence, the value of τ_{exc} is incremented by incrementing the number of C elements. Double-quantum coherence is reconverted to longitudinal magnetization by applying the same number of C cycles as that in the excitation step. The overall phase of the first cycle in the reconversion step is obtained by adding the $2\pi/7$ phase to the phase of the last cycle in the excitation step. The overall phases of the following cycles are incremented by $2\pi/7$, analogous to the excitation step. If the free precession interval of double-quantum coherence is incremented, or contains additional pulses such as π-pulses, determination of the phase of the reconversion cycles requires more laborious considerations, as described in ref 31. Transverse, observable magnetization is acquired after a strong $\pi/2$-pulse after the DQC reconversion block (not shown). This $\pi/2$-pulse should be incorporated into the overall phase cycling scheme.

2.3. SPC-5. The SPC-5 rf pulse sequence[29] is shown in Figure 2c. As in the case of the C7 and POST-C7 sequences, it is assumed that magnetization is prepared along the z-axis $(\hat{S}_{jz} + \hat{S}_{kz})$ prior to application of the sequence.

The SPC-5 sequence consists of five rf cycles C, each with an overall phase, ϕ, incremented in steps of $2\pi/5$. We note that the rf cycle C used in SPC-5 is the same as the rf cycle used in POST-C7 (Figure 2b, panel II).

The sequence of five cycles is supercycled by another five cycles, each one denoted $\bar{C}$. $\bar{C}$ is a phase-shifted C cycle, obtained by adding an overall phase of π to each pulse in the cycle C. SPC-5 is designed such that $5C + 5\bar{C}$ cycles occupy four rotational periods, $4 \times \tau_r$. The rf amplitude is adjusted to satisfy the condition $\omega_{rf}^S = 5 \times \omega_r$.

As in the case of C7 and POST-C7, the SPC-5 sequence excites double-quantum coherence by incrementing the number of C, $\bar{C}$ cycles during the excitation step. The duration of the double-quantum coherence excitation interval is denoted by τ_{exc} in Figure 2. Double-quantum coherence is reconverted to longitudinal magnetization by applying the same number of C, $\bar{C}$ cycles as that in the excitation step and transferred to observable transverse magnetization by a final $\pi/2$-pulse (not shown).

2.4. RN_n^ν Recoupling Sequences. The family of R recoupling sequences[30] are shown in Figure 2d. As in the case of previous sequences (C7, POST-C7, and SPC-5), the R family of sequences excites double-quantum coherence from a state of longitudinal magnetization, i.e., $(\hat{S}_{jz} + \hat{S}_{kz})$.

In the notation RN_n^ν, N is the number of RR′ elements in the sequence and n is the total number of rotor periods, τ_r, that the sequence occupies. The parameter ν determines an overall rf phase, ϕ, for the R and R′ elements and is obtained through the relation

$$\phi = \frac{180\nu}{N} \qquad (5)$$

Any R sequence is built around a single rf block, consisting of two entities, denoted as R and R′. R′ is obtained from R by adding an overall phase of $(2\pi - \phi)$ to all internal phases in R. In the presented study, R consists of two pulses of flip angles $\{\pi/2, 3\pi/2\}$, with rf phases $\{x, \bar{x}\}$.

Excitation of double-quantum coherence is achieved by incrementing the number of RR′ elements. Double-quantum coherence is reconverted to longitudinal magnetization by applying the same number of RR′ elements as that in the excitation step. Longitudinal magnetization is transferred to observable magnetization by a final $\pi/2$-pulse (not shown). The reconversion part of the sequence may also be held constant, i.e., containing a constant number of RR′ elements. The resulting form of the excitation curve from such an asymmetric procedure is different from the symmetric procedure and produces a larger range of amplitudes, as discussed in the work by Carravetta et al.[43]

The sequence may employ supercycling[43] to improve compensation of CSA effects and rf mis-set errors. The simplest form of a two-step supercycle is obtained by shifting the overall phase of one full execution of the sequence to another with π. Such a supercycle is denoted $SR = [RN_n^\nu]_0[RN_n^\nu]_\pi$, where $[...]_\phi$ denotes an overall phase shift through the angle ϕ.

In this study, two different R sequences are discussed: $R14_2^6$ and $SR22_4^9$.

3. Experimental Methods and Samples

3.1. Experimental Procedure. All NMR experiments were performed on a home-built spectrometer,[44] operating at a proton frequency of 400.6 MHz. A doubly tuned Chemagnetics MAS probe was used, with a rotor diameter of 5 mm. To minimize the effect of rf inhomogeneity, extra spacers were used to reduce the sample volume from $\simeq 130\ \mu L$ to $\simeq 86\ \mu L$.

The ^1H $\pi/2$-pulse length was 4.6–5.5 μs in all experiments. The cross-polarization time was 2 ms. The proton decoupling field during acquisition was 110–140 kHz. The ^{13}C $\pi/2$-pulse length was 6.25 μs in all experiments. The ^{13}C field, under excitation and reconversion of double-quantum coherence, was calibrated to be 40 kHz, resulting in the following sample spinning speeds for different rf sequences: DRAWS, 4705 Hz; POST-C7, 5714 Hz; SPC-5, 8000 Hz; $R14_6^2$, 5714 Hz; and $R22_4^9$, 7272 Hz. In the ^{13}C channel, a simple z-filter was employed before and after the recoupling sequence. The z-filter stores the magnetization along the z-axis in the rotating frame for a short period, $\tau_{free} = 2 \times \tau_r$, under which the decoupler is turned off. A conventional Hahn spin–echo sequence[45] was employed before acquisition of the signal.

In the case of the $R14_6^2$ and the $R22_4^9$ sequence, the parameter ϕ (eq 5) was optimized as follows: at a double-quantum coherence excitation time τ_{exc}, which was estimated to be optimal, an array of experiments that varied the value of ϕ in increments of 0.1° and within ±1° from the theoretical ϕ were acquired. The ϕ value corresponding to the experiment showing the largest peak integral was chosen. This procedure differs slightly from the recommended procedure in ref 43. The theoretical ϕ value is $\simeq 73.64°$ in the case of the $R22_4^9$ sequence and $\simeq 77.14°$ for $R14_2^6$.

Double-quantum coherence excitation efficiencies, ϵ^{DQ}, were calculated as the ratio of the peak intensity from signals going through a double-quantum coherence state, S^{DQ}, to the peak intensity of a single-

(43) Carravetta, M.; Eden, M.; Johannessen, O. G.; Luthman, H.; Verdegem, P. J. E.; Lugtenburg, J.; Sebald, A.; Levitt, M. H. *J. Am. Chem. Soc.* **2001**, *123*, 10628.
(44) Gladden, J.; Drobny, G. P., unpublished results.
(45) Hahn, E. L. *Phys. Rev.* **1950**, *80*, 580.

Table 2. Spin Interaction Parameters Corresponding to the Samples in Figure 3[a]

	I. alanine		II. oxalic acid		III. alanine		IV. malonic acid		V. AGG		VI. succinic acid	
	$j = 2$	$k = 3$	$j = 1$	$k = 2$	$j = 1$	$k = 3$	$j = 1$	$k = 3$	$j = $ 1-A	$k = $ 1-G	$j = 1$	$k = 4$
δ^{iso}/ppm	15.5	−15.5	0	0	78.7	−78.7	0.2	−0.2	0.8	−1.1	0	0
δ^{aniso}/ppm	−19.7	−11.7	88.15	88.15	−72.0	−11.7	−67.3	70.3	84	84	76.95	76.95
η	0.44	0.76	0.126	0.126	0.84	0.76	0.92	0.85	0.69	0.74	0.89	0.89
Ω^{PC}/deg	82, 24, 29	39, 77, −53	−5, −110, −90	−5, 70, −90	0, 0, 0	39, 77, −53	0, 0, 0	0, 0, 0	0, 110, 226	290, 97, 291	0, 0, 0	0, 0, 0
Ω^{PC}_{jk}/deg	0, 78, −35		0, 0, 0		0, 0, 0		0, 0, 0		0, 110, 226		0, 0, 0	
r_{jk}/Å	1.53		1.53		2.51		2.54		3.19		3.91	

[a] All parameters were taken from the literature, as referenced in the text. Molecular site assignment is as indicated in Figure 3.
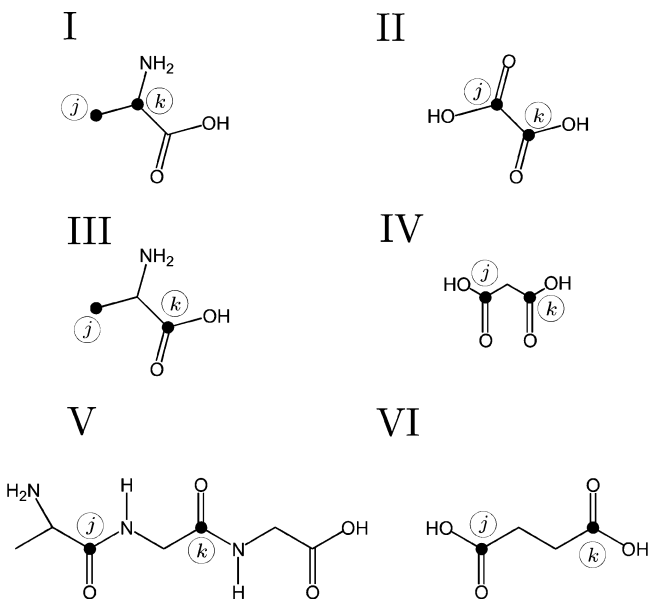
Figure 3. Samples used in this study: I, [2,3-^{13}C$_2$]-alanine; II, [1,2-^{13}C$_2$]-oxalic acid; III, [1,3-^{13}C$_2$]-alanine; IV, [1,3-^{13}C$_2$]-malonic acid; V, [1-^{13}C]-A-[1-^{13}C]-GG; and VI, [1,4-^{13}C$_2$]-succinic acid. The solid circle (●) indicates the ^{13}C spin label. In the assignments *j* and *k*, *j* refers to the most chemically shielded site. Internuclear distances and chemical-shift parameters are found in Table 2.

quantum signal, S^{SQ}, acquired before the recoupling sequence, i.e., $\epsilon^{DQ} = S^{DQ}/S^{SQ}$. The S^{SQ} signal was acquired with a pulse sequence where the *z*-filters and the spin−echo pulse were intact, while the recoupling sequence was omitted. The ϵ^{DQ} values were corrected for natural abundant spins, when present. All experimental and simulated data were processed with the Gullringen program.[40]

3.2. Samples. A wide range of molecular compounds, shown in Figure 3, were used in this study. In the figure, isotopically labeled molecular sites are indicated by a solid circle (●). The *j* and *k* labels identify two chemical sites and refer to chemical-shift properties, where *j* denotes the most shielded site. Relevant spin-dynamical and geometrical parameters for the samples in Figure 3 are listed in Table 2. The sample array exhibits a wide range of internuclear distances and CSAs. Internuclear distances vary from 1.53 Å in the case of [2,3-^{13}C$_2$]-alanine (Figure 3, sample I) to 3.91 Å in the case of [1,4-^{13}C$_2$]-succinic acid (Figure 3, sample VI). Relatively small CSAs are found in the alanine samples, whereas relatively large CSAs are found in the rest of the samples.

The following discussion describes the preparation of the samples I−VI.

3.2.1. Sample I. [2,3-^{13}C$_2$]-L-alanine[46,47] was purchased from Cambridge Isotope Laboratories, Inc. (Andover, MA) with 99% ^{13}C purity and was neither purified nor diluted.

3.2.2. Sample II. [1,2-^{13}C$_2$]-oxalic acid[48,49] was purchased from Cambridge Isotope Laboratories, Inc. (Andover, MA) with 99% ^{13}C purity and was neither purified nor diluted.

3.2.3. Sample III. DL-[1,3-^{13}C$_2$,^{15}N]-alanine[46,47] was purchased from Cambridge Isotope Laboratories, Inc. (Andover, MA) with 99% ^{13}C and 99% ^{15}N purity, and the material was neither purified nor diluted.

3.2.4. Sample IV. [1,3-^{13}C$_2$]-malonic acid[50,51] was purchased from Isotec, Inc., and was diluted to 5% with unlabeled malonic acid.

3.2.5. Sample V. [1-^{13}C]-A-[1-^{13}C]-GG[52] (alanine−glycine−glycine) was synthesized and purified as discussed in the work by Shaw et al.[53] To reduce the effect of intermolecular dipole−dipole couplings, the compound was diluted to 10% with unlabeled AGG and subsequently recrystallized.

3.2.6. Sample VI. [1,4-^{13}C$_2$]-succinic acid[54] was purchased from Isotec, Inc., and diluted to 5% with unlabeled succinic acid.

3.3. Spin Dynamical Calculations. Theoretical double-quantum buildup curves were calculated using the simulation program SIMPSON,[39] together with a Windows-based user interface called Gullringen.[40] Simulations were performed using the direct algorithm,[39] omitting relaxation. In general, a set of 54 Euler angles, specified by the Zaremba−Conroy−Wolfsberg[55−57] scheme, and 5 γ angles were used to simulate a powder sample of randomly oriented crystallites. The simulations were tested using larger crystallite sets, to confirm convergence. Simulated buildup curves were fitted to the experimental results by scaling them vertically, using a numerical factor *A*, and multiplying the simulated points with an exponential decay function, using a decay rate constant λ, as discussed below. The parameters *A* and λ are tabulated in Table 3, with the double-quantum excitation efficiency (ϵ^{DQ}) and estimated internuclear distances (r_{jk}), which are discussed below.

3.3.1. Double-Quantum Coherence Excitation Efficiencies. In Table 3, along with other experimental parameters, experimentally acquired ϵ^{DQ} values are tabulated for samples I−VI, shown in Figure 3, using different recoupling sequences. The theoretical excitation efficiency values, before applied damping, are shown in parentheses.

For samples containing directly bonded ^{13}C atoms, i.e., [2,3-^{13}C$_2$]-alanine (sample I) and [1,2-^{13}C$_2$]-oxalic acid (sample III), the excitation efficiency using POST-C7, SPC-5, R14$_6^2$, and $SR22_4^9$ are well above 50%. In these samples, the DRAWS sequence shows an excitation efficiency of ∼30%.

For samples with intermediate internuclear distances, as in the case of [1,3-^{13}C$_2$]-alanine (sample III), the excitation efficiencies for POST-

(46) Naito, A.; Ganapathy, S.; Akasaka, K.; McDowell, C. A. *J. Chem. Phys.* **1981**, *74*, 3190.
(47) Simpson, H. J., Jr.; Marsh, R. E. *Acta Crystallogr.* **1966**, *63*, 1267.
(48) Ahmed, F. R.; Cruickshank, D. W. J. *Acta Crystallogr.* **1953**, *6*, 385.
(49) Griffin, R.; Pines, A.; Pausak, S.; Waugh, J. S. *J. Chem. Phys.* **1975**, *63*, 1267.
(50) Jagannathan, N. R. *Magn. Reson. Chem.* **1989**, *27*, 941.
(51) Jagannathan, N. R.; Rajan, S. S.; Subramanian, E. *J. Chem. Crystallogr.* **1994**, *24*, 75.
(52) Lalitha, V.; Subramanian, E.; Bordner, J. *Indian J. Pure Appl. Phys.* **1985**, *23*, 506.
(53) Shaw, W. J.; Long, J. R.; Dindot, J. L.; Campbell, A. A.; Stayton, P. S.; Drobny, G. P. *J. Am. Chem. Soc.* **2000**, *122*, 1709.
(54) Verweel, H. J.; MacGillavry, C. H. *Nature* **1938**, *142*, 161.
(55) Zaremba, S. K. *Annali di Matematica Pura Ed Applicata* **1966**, *73*, 293.
(56) Conroy, H. *J. Chem. Phys.* **1967**, *47*, 5307.
(57) Cheng, V. B.; Suzukawa, H. H.; Wolfsberg, M. *J. Chem. Phys.* **1973**, *59*, 3992.

Table 3. Experimentally Acquired Parameters for the Samples in Figure 3, Using the rf Sequences Shown in Figure 2^a

	I. alanine	II. oxalic acid	III. alanine	IV. malonic acid	V. AGG	VI. succinic acid
			POST-C7			
A	1.0	1.0	1.3			
λ/Hz	180	140	122			
ϵ^{DQ}	0.62 (0.72)	0.52 (0.65)	0.38 (0.66)			
r_{jk}/Å	1.51 ± 0.06	1.59 ± 0.04	2.61 ± 0.38			
			SPC-5			
A	1.0	1.0	1.0			
λ/Hz	254	130	124			
ϵ^{DQ}	0.62 (0.72)	0.55 (0.65)	0.32 (0.65)			
r_{jk}/Å	1.54 ± 0.02	1.68 ± 0.09	2.39 ± 0.18			
			R14$_2^6$			
A	1.1	1.0	1.0			
λ/Hz	250	126	132			
ϕ/deg	77.0	76.8	77.0			
ϕ'/deg	77.1	77.14	77.03			
ϵ^{DQ}	0.64 (0.71)	0.56 (0.65)	0.45 (0.62)			
r_{jk}/Å	154. ± 0.02	1.59 ± 0.02	2.38 ± 0.04			
			SR22$_4^9$			
A	1.0	1.0	1.0	1.0	1.0	1.2
λ/Hz	206	140	118	184	106	87
ϕ/deg	73.6	73.6	73.7	73.5	73.5	73.6
ϕ'/deg	73.55	73.52	73.46	73.64	73.46	73.53
ϵ^{DQ}	0.59 (0.72)	0.61 (0.64)	0.40 (0.64)	0.41 (0.65)	0.28 (0.40)	0.25 (0.43)
r_{jk}/Å	1.54 ± 0.02	1.58 ± 0.03	2.46 ± 0.1	2.56 ± 0.06	3.16 ± 0.03	3.72 ± 0.07
			DRAWS			
A	0.85	1.0	1.0	1.0	1.0	1.2
λ/Hz	160	140	125	177	107	103
ϵ^{DQ}	0.31 (0.45)	0.32 (0.41)	0.27 (0.39)	0.27 (0.46)	0.26 (0.44)	0.24 (0.40)
r_{jk}/Å	1.53 ± 0.08	1.69 ± 0.06	2.46 ± 0.12	2.67 ± 0.19	3.22 ± 0.04	3.75 ± 0.06

^{a} A is the vertical scaling factor, λ the decay rate constant, and ϵ^{DQ} the double-quantum excitation efficiency in the experiment (the theoretical efficiencies, before any dampening, are given in parentheses); r_{jk} is the estimated distance (in angstroms). For R14 and R22, the parameter ϕ denotes the experimentally determined value, as discussed in the text; the parameter ϕ' corresponds to the local minimum in the contour plots, which is used to estimate r_{jk}.

C7, SPC-5, R14$_2^6$, and SR22$_4^9$ decrease to 32%−45%. For this sample, the DRAWS sequence shows an excitation efficiency of 27%.

Sample IV (malonic acid) has larger CSAs than [1,3-^{13}C$_2$]-alanine but has a comparable internuclear distance. The excitation efficiency in the case of the DRAWS sequence was 27% when applied to malonic acid. For the SR22$_4^9$ sequence, the excitation efficiency was ∼40%.

Samples V (AGG) and VI ([1,4-^{13}C$_2$]-succinic acid) have large CSAs and relatively long internuclear distances. In these samples, it was found, by inspecting simulations, that the only recoupling sequences that would excite double-quantum coherence with a practical excitation efficiency were SR22$_4^9$ and DRAWS. The acquired experimental excitation efficiencies in these samples were 24%−28% for both SR22$_4^9$ and DRAWS.

Figure 4 shows double-quantum buildup curves for two pulse sequences, DRAWS and SR22$_4^9$, applied to [2,3-^{13}C$_2$]-alanine and AGG. The DRAWS buildup curve acquired for [2,3-^{13}C$_2$]-alanine (Figure 4a), a sample with small CSAs and a large dipole−dipole coupling constant, shows a maximum double-quantum efficiency of $\epsilon^{DQ} = 31\%$. When DRAWS is applied to the sample AGG (Figure 4b), which is a sample with large CSAs and a somewhat small dipole−dipole coupling constant, the ϵ^{DQ} value drops slightly, from 31% to 26%. The trend is different for the pulse sequence SR22$_4^9$. In Figure 4c and d, SR22$_4^9$ is applied on [2,3-^{13}C$_2$]-alanine and AGG, respectively. In the case of [2,3-^{13}C$_2$]-alanine, a maximum double-quantum efficiency of $\epsilon^{DQ} = 59\%$ is obtained. In the case of AGG, the ϵ^{DQ} value drops drastically, to 28%.

3.3.2. Estimation of Internuclear Distances. By fitting simulated data to experimental data, internuclear distances were estimated for the sample array in Figure 3. To fit the experimental data, the two model parameters λ and A were employed in the theoretical analysis, as

$$a^{sim'}(t) = A a^{sim}(t) \exp\{-\lambda t\} \tag{6}$$
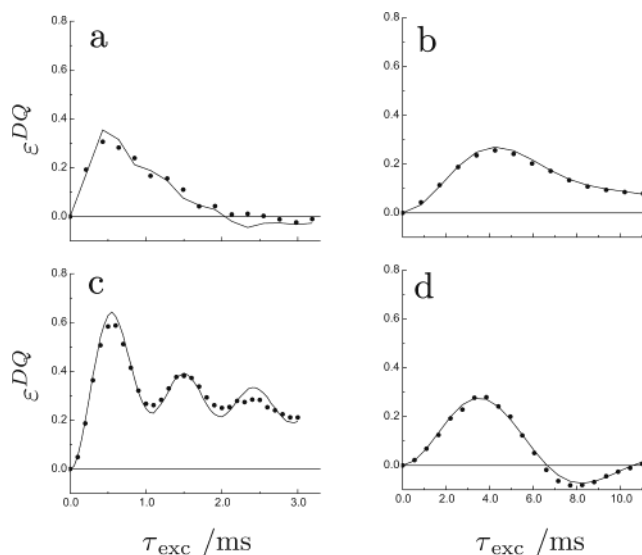
Figure 4. Experimental points and best-fit simulations (solid line) of double-quantum buildup curves. In panels a and b, the DRAWS pulse sequence was applied on [2,3-^{13}C$_2$]-alanine and AGG, respectively. In panels c and d, the SR22$_4^9$ sequence was applied on the same samples. In alanine, the X-ray internuclear distance is $r_{jk} = 1.53$ Å, and in AGG, $r_{jk} = 3.19$ Å. In the case of [2,3-^{13}C$_2$]-alanine, the DRAWS curve was fitted to a distance of 1.53 (± 0.08) Å, and the SR22$_4^9$ curve was fitted to a distance of 1.54 (± 0.02) Å in the case of alanine. In AGG, a distance of $r_{jk} = 3.22$ (± 0.04) Å was obtained for DRAWS; a distance of $r_{jk} = 3.16$ (± 0.03) Å was obtained for SR22$_4^9$.

where a^{sim} is simulated data. The parameter A is an arbitrary scaling factor, representing uncontrollable experimental imperfections, such as insufficient heteronuclear decoupling, whereas λ is introduced to model

relaxation of the double-quantum coherence. In this study, A is determined by visual inspection, whereas the internuclear distance, r_{jk}, is obtained by minimization of the χ^2 value, as discussed in Press et al.[58] The value of λ is obtained from the sum of the line widths of the two isotropic peaks in the single-quantum spectrum. The exact value of λ is not critical when the double-quantum dynamics is dominated by the dipole−dipole coupling (short internuclear distances); however, the value of λ may interfere with internuclear distance estimations if the spin dynamics is dominated by double-quantum relaxation (long internuclear distances). In the case of very long internuclear distances, this parameter should be explicitly measured in a separate double-quantum coherence relaxation experiment (see Karlsson et al.[31])

The χ^2 relation is given by

$$\chi^2 = \sum_i^N \frac{(a_i^{\text{exp}} - a_i^{\text{sim}'})^2}{\sigma^2} \tag{7}$$

where a_i^{exp} are experimental points, $a_i^{\text{sim}'}$ are simulated points (after application of A and exponential dampening, as in eq 6), and σ^2 is the variance.

To assign confidence limits on the estimated internuclear distance, the variance is calculated as

$$\sigma^2 = \sum_i^N \frac{(a_i^{\text{exp}} - a_i^{\text{bestfit}})^2}{N - M} \tag{8}$$

where a_i^{bestfit} are simulated points of the best fit, obtained by assigning an arbitrary variance of 1 in eq 7 and searching for the smallest χ^2 value (as a function of the dipole−dipole coupling constant, $b_{jk}/2\pi$), N is the total number of points, and M is the number of fitting parameters. In our case, $M = 2$, corresponding to λ and A. The χ^2 relation in eq 7 is finally recalculated using the variance obtained from eq 8.
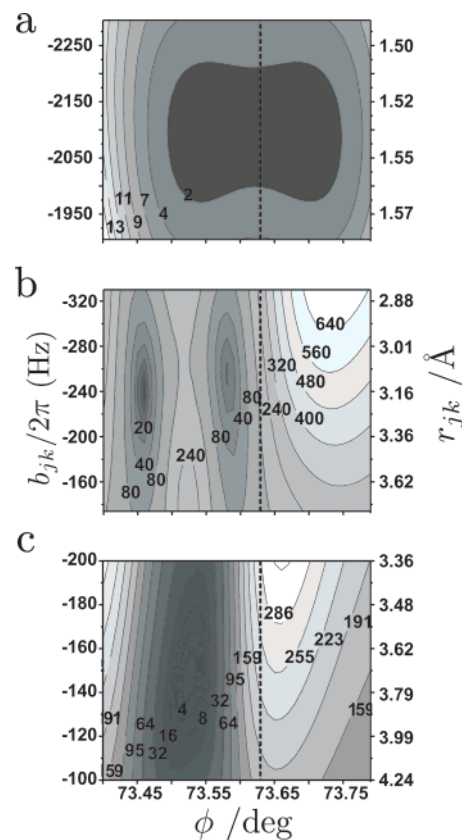
Following this procedure, the simulated buildup curves of various dipolar couplings are considered good fits if $\chi^2 < (N - M)\sqrt{2}$, as discussed in ref 58. The parameters A, λ, ϵ^{DQ}, and r_{jk} are tabulated in Table 3.

For samples with directly bonded nuclei (i.e., alanine (sample I) and oxalic acid (sample II)), the estimated distances using the DRAWS, POST-C7, SPC-5, $R14_2^6$, and $SR22_4^9$ sequences were in the range of 1.51−1.69 Å.

For samples with intermediate distances (i.e., alanine (sample III) and malonic acid (sample IV), whose internuclear distances (X-ray) are 2.51 and 2.54 Å, respectively), the estimated distances obtained were in the range of 2.34−2.51 Å.

For samples with long internuclear distances (i.e., AGG (sample V) and succinic acid (sample VI)), estimated distances were obtained with the DRAWS and $SR22_4^9$ sequences only. In the case of AGG, with an X-ray distance of 3.19 Å, the DRAWS sequence estimated a distance of 3.22 ($\pm$ 0.04) Å, whereas the $SR22_4^9$ sequence gives a distance of 3.16 ($\pm$ 0.03) Å. In succinic acid, with an internuclear distance of 3.91 Å (X-ray), DRAWS and $SR22_4^9$ estimated the distances to be 3.75 ($\pm$ 0.06) and 3.72 ($\pm$ 0.07) Å, respectively.

3.3.3. R Sequences and χ^2-Plots. In this section, the reduced chi-square, χ_ν^2, is investigated as a function of the direct dipole−dipole coupling constant ($b_{jk}/2\pi$) and the pulse sequence parameter ϕ (eq 5). The χ_ν^2 value is obtained by dividing the calculated χ^2 value (from eqs 7 and 8) by the term ν ($\nu = N - M$, where N is the number of experimental points and M is the number of fitting parameters). A best fit gives a reduced chi-square value of $\chi_\nu^2 = 1$. Figure 5 shows contour

(58) Press, W. H.; Flannery, B. P.; Teukolsky, S. A.; Vetterling, W. T. *Numerical Recipes in C. The Art of Computing*; Cambridge University Press: Cambridge, U.K., 1986.

Figure 5. Reduced χ^2 (χ_ν^2) contour plots of $SR22_4^9$ simulations of experimental data, as a function of ϕ and the dipole−dipole coupling constant, $b_{jk}/2\pi$ (left y-axis). The internuclear distance, r_{jk} (right y-axis), was calculated from the dipole−dipole constant, b_{jk}. The samples were (a) [2,3-^{13}C$_2$]-alanine, (b) AGG, and (c) [1,4-^{13}C$_2$]-succinic acid. The dashed line in each plot corresponds to the theoretical ϕ value for the $R22_4^9$ sequence.

plots over the χ_ν^2 region, as a function of $b_{jk}/2\pi$ and ϕ, for the pulse sequence $SR22_4^9$, applied to alanine (sample I) (panel a), AGG (sample V) (panel b), and succinic acid (sample VI) (panel c). The dashed line in each figure indicates the value of the theoretically computed ϕ, which, in the case of $SR22_4^9$, is equal to $\simeq 73.64°$. Each contour plot has a minimum, corresponding to a internuclear distance r_{jk}, and a phase ϕ', as tabulated in Table 3.

Figure 5a indicates that a wide range of ϕ values results in the same estimate of the internuclear distance for alanine (sample I), 1.53 ($\pm$ 0.02) Å.

Figure 5b shows the χ_ν^2 plot for AGG, which is a sample with large CSAs and a small dipole−dipole coupling constant. The plot shows two minima: one at $\phi' = 73.46°$ and the other at $\phi' = 73.58°$. The minima at $\phi' = 73.46°$ corresponds to an internuclear distance of 3.16 ($\pm$ 0.03) Å. The minima at $\phi' = 73.58°$ is not considered a good fit, because the χ^2 value is greater than $(N - M)\sqrt{2}$.

Figure 5c shows the χ_ν^2 plot for succinic acid. We observe one distinct minimum, at $\phi' = 73.53°$, corresponding to an internuclear distance of 3.72 ($\pm$ 0.07) Å. The plot in Figure 5c shows a slight tilt of the contour valley, indicating a weak correlation of the parameter ϕ to the estimated internuclear distance r_{jk}.

We observe that the experimentally optimized value of ϕ, which is listed in Table 3, generally does not correspond to either the theoretical ϕ value or the ϕ' value at the minimum in the χ_ν^2 plot. This unpredictable behavior is due to the experimental uncertainty in the ϕ-phase, but it is also caused by induced phase accumulations due to the CSA, as discussed in ref 43.

4. Theory and Simulations

In this section, the performance of individual pulse sequences are analyzed by computer calculations and compared to trends in the experimental data, as reported in Table 3.

Numerical calculation of the evolution of the density matrix is straightforward and gives insight into how a pulse sequence performs on a particular spin system and under controlled experimental conditions. In such calculations, the spin system is characterized in terms of internuclear distances and chemical-shift tensors, whereas experimental conditions are characterized by rf fields and sample spinning speeds. Numerical calculations can give information on how sensitive a particular sequence is to any of these parameters. However, the *origin* of such problems is not answered by this type of calculation, nor does the calculation explain why a particular rf-pulse sequence performs better than another. As an attempt to quantify the breakdown of a particular pulse sequence, we also investigate the properties of the spin dynamics in the double-quantum subspace.

4.1. Computer Simulations. Density-matrix calculations of the spin dynamics occurring under the application of a sequence of rf pulses give a direct measure of the experimental outcome under controlled experimental circumstances. The information from such calculations is used to estimate molecular and experimental parameters, such as CSAs, dipole−dipole couplings, properties of the applied rf field, and sample spinning. Other effects, such as magnetic-field inhomogeneities and relaxation of transverse or longitudinal magnetization, are generally more difficult to treat and are not discussed in this paper. Below, we outline the steps for calculating the spin dynamics, using density-matrix calculations.

The calculation starts by the definition of a total spin Hamiltonian, H_{tot}:

$$H_{\text{tot}} = H_{\text{int}} + H_{\text{ext}} \quad (9)$$

where H_{int} represents internal spin interactions, such as chemical shifts and direct dipole−dipole couplings, and H_{ext} represents external spin interactions, such as an externally applied rf field.

In general, the time evolution of the quantum mechanical state of the spin-system ensemble, represented by the density matrix ρ, is given by the Liouville von Neumann equation:

$$\left(\frac{\text{d}}{\text{d}t}\right)\rho = -i\hbar[H, \rho] \quad (10)$$

where $\hbar = h/2\pi$. The Liouville equation of motion is a description of how the ensemble of spin states evolves with time under the Hamiltonian, H. The evolution of the state of the spin system, in terms of the spin-density operator, may be written more conveniently as

$$\rho(t_b) = U(t_b, t_a)\rho(t_a)U^{\dagger}(t_b, t_a) \quad (11)$$

where U is the propagator, or evolution operator, formally obtained as

$$U(t_b, t_a) = \hat{T} \exp\left\{-i \int_{t_a}^{t_b} H_{\text{tot}}(t) \, \text{d}t\right\} \quad (12)$$

where $\hat{T}$ is the Dyson time ordering operator. Equation 11 is a description of how the state of the spin system is translated, or propagated, from time t_a to t_b. As eqs 11 and 12 show, the

propagation of the spin system in time depends solely on the actual form of the spin Hamiltonian, H_{tot}.

Limiting the discussion to the case of an isolated pair of spin-$^1/_2$ nuclei, j and k, rotating at the magic angle, the internal part of the Hamiltonian may be written as

$$H_{\text{int}} = H_j^{\text{CS}}(t, \Omega) + H_k^{\text{CS}}(t, \Omega) + H_{jk}^{\text{spin−spin}}(t, \Omega) \quad (13)$$

where H_j^{CS} and H_k^{CS} are the chemical-shift interactions and $H_{jk}^{\text{spin−spin}}$ is the homonuclear spin interaction. The Euler angle triplet, Ω, indicates that these interactions are dependent on the molecule's orientation, with respect to a laboratory frame L, defined by the external magnetic field B_0. (See the work of Levitt et al.[59] for explicit expressions for these terms.)

When the full Hamiltonian is defined, the propagator (eq 12) is numerically calculated and employed in eq 11, to yield the evolution of the spin system. At any point in time, the NMR time domain signal, $s(t)$, is obtained as

$$s(t) = \text{Tr}\{Q_{\text{det}}\rho(t)\} \quad (14)$$

where Q_{det} is the detection operator and $\rho(t)$ is the spin-density operator.

In this paper, we used the simulation engine SIMPSON[39] to calculate the time domain NMR signal. Spin interaction parameters were controlled by the Windows interface Gullringen.

4.1.1. Gullringen and SIMPSON. Spin dynamical calculations were performed using the programs SIMPSON[39] and Gullringen.[40] The calculations were run on a Windows 2000 platform.

Gullringen is a program suitable for defining molecular geometry and NMR interaction tensors, as well as processing experimental and simulated data. Gullringen provides the user with a friendly interface to SIMPSON. In the program, molecular geometry is defined in terms of atomic coordinates and chemical bonds. From such geometry, the program subsequently allocates and calculates relevant NMR interaction parameters, such as the orientation and magnitude of dipole−dipole couplings and the orientation of CSA tensors. The program allows these parameters to be passed on to external modules responsible for spin-dynamical calculations, e.g., SIMPSON. Gullringen can be downloaded from the Drobny group homepage (http://depts.washington.edu/drobnygp/). It should be noted that all simulations presented in this paper can be obtained without using this program.

SIMPSON is a program used for simulations of the spin dynamics in solid-state experiments under MAS. SIMPSON takes input files containing relevant spin interaction parameters and a detailed description of the relevant pulse sequence. Input files to SIMPSON are written in a well-established script language called Tcl.[60] The inner workings of SIMPSON are beyond the scope of this paper. Briefly, SIMPSON constructs the relevant Hamiltonian (eq 9), numerically calculates the propagator (eq 12), and finally calculates the NMR time domain signal for a single crystallite orientation (as in eq 14). In general, a powder average is calculated and SIMPSON takes into account

(59) Levitt, M. H.; Raleigh, D. P.; Creuzet, F.; Griffin, R. G. *J. Chem. Phys.* **1990**, *92*, 6347.
(60) Welch, B. B. *Practical Programming in Tcl and Tk*; Prentice Hall: Englewood Cliffs, NJ, 1995.

Table 4. Spin Interaction Parameters Employed in the Simulations Presented in Figure 6[a]

sample	$b_{jk}/2\pi$ (Hz)	shift parameter (ppm)			
		δ_j^{iso}	δ_k^{iso}	$\delta_{j,k}^{aniso}$	$\eta_{j,k}$
A	−200	50	−50	50	0.5
B	−200	50	−50	100	0.5

[a] The Euler angle triplet, $\Omega^{PC} = \{\alpha^{PC}, \beta^{PC}, \gamma^{PC}\}$, relating the PAS frame of each chemical-shift tensor to a crystal defined frame, was equal to {0, 0, 0}. The crystal frame was chosen to be coincident with the PAS frame of the dipole−dipole coupling tensor.

the necessary weighting of crystallites, depending on what type of simulation technique and crystallite set is used.

4.1.2. Spin Dynamical Parameters. Table 4 shows two different sets of spin dynamical parameters employed in the discussion below. Samples A and B represent a pair of ^{13}C spins with an active dipole−dipole coupling constant ($b_{jk}/2\pi = -200$ Hz, corresponding to an internuclear distance of $r_{jk} = 3.36$ Å). In both samples, the isotropic chemical shifts were $\delta_j^{iso} = +50$ ppm and $\delta_k^{iso} = -50$ ppm, and the asymmetry parameters were $\eta_j = \eta_k = 0.5$. In sample A, both CSAs were 50 ppm, whereas in sample B, both CSAs were 100 ppm. Sample B corresponds to a sample with two relatively large CSAs. In both cases, the orientation of chemical-shift tensors has been chosen to be coincident with the principal axis system (PAS) of the dipole−dipole coupling tensor. In practice, this is generally not the case, and it should be noted that the orientation of the CSA tensors plays a major role when their magnitude is large, with respect to other interactions.

A discussion of the performance of different pulse sequences using the spin interaction parameters in Table 4 is given below.

4.1.3. Simulation Setup. Computer calculations of the spin dynamics for the rf-pulse sequences DRAWS, POST-C7, SPC-5, R14$_2^6$, and $SR22_4^9$ were produced by the Gullringen program and the SIMPSON simulation engine. The calculations are presented in the form of double-quantum coherence buildup curves, as a function of the sample rotation speed, ω_r. Referring to Figure 1, a double-quantum coherence buildup curve is obtained by incrementing the time for excitation of double-quantum coherence, τ_{exc}, and keeping $\tau_{rec} = \tau_{exc}$. The single-quantum peak integral, obtained in t_2, is plotted as a function of τ_{exc}. If the resulting integrals are divided by the peak integral acquired from an experiment in which the recoupling sequence is absent, i.e., a pure single quantum experiment, the integral at a certain time τ_{exc} represents the excitation efficiency of double-quantum coherence at that time point.

In this study, double-quantum coherence buildup curves are acquired as a function of the magnitude of the involved CSAs and of the sample rotation speed ω_r.

4.1.4. Simulation Results. Figure 6 shows contour plots of the double-quantum excitation efficiency, as a function of the sample spinning speed, the excitation time, and the magnitude of the CSAs (panels a and b), for the pulse sequences POST-C7, SPC-5, $SR22_4^9$, and DRAWS. Figure 6a and b correspond to samples A and B in Table 4, respectively. In each contour plot, the x-axis is the sample rotation frequency $\omega_r/2\pi$ (bottom) and the corresponding applied rf field strength $\omega_{rf}^S/2\pi$ (top) (both given in units of kHz). The y-axis is the excitation time for double-quantum coherence, τ_{exc}. In all plots, the maximum x-value is obtained at an rf field corresponding to a S-spin nutation frequency of $\omega_{rf}^S/2\pi = 100.0$ kHz. The mini-
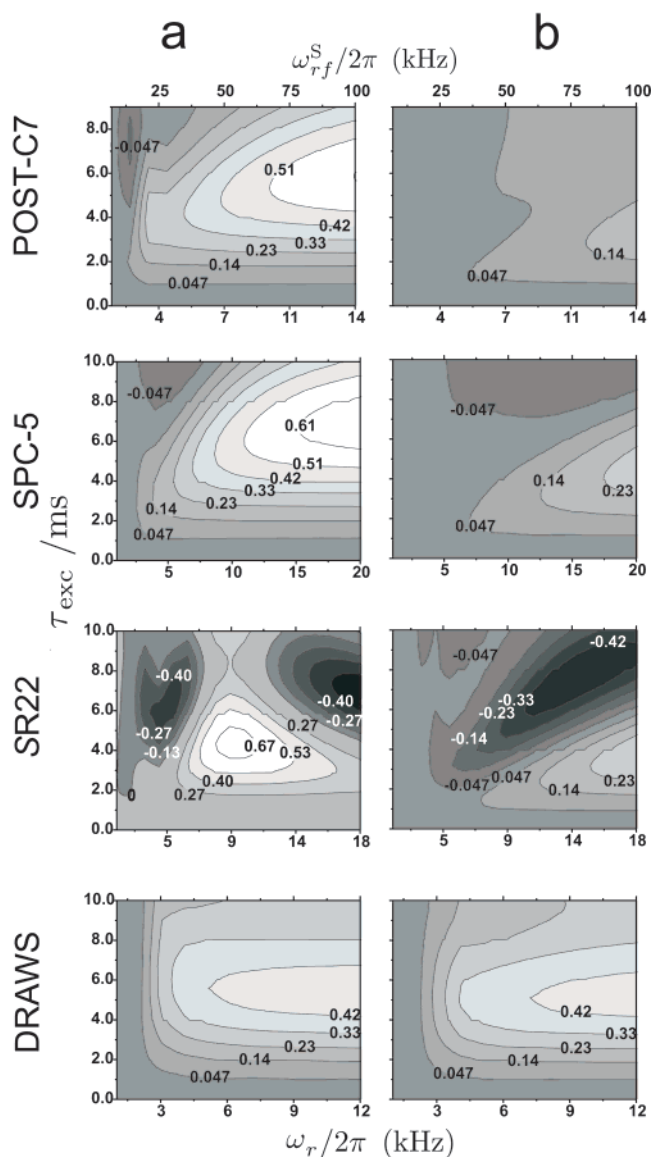
Figure 6. Double-quantum coherence buildup curves for the pulse sequences POST-C7, SPC-5, SR22, and DRAWS, plotted as a function of spinning speed, ω_r, and chemical shifts, a and b. In the figure, a and b refer to the parameters in Table 3. The y-axis in each plot shows excitation time τ_{exc} (in milliseconds), the bottom x-axis shows the spinning speed (in kHz), and the top x-axis shows the corresponding rf field (in kHz). The contour levels correspond to the absolute excitation efficiency.

mum x-value is obtained at a sample rotation frequency of 1.0 kHz. We observe that the ratio ω_{rf}^S/ω_r differs for different rf sequences. We also observe that the sequences DRAWS, POST-C7, and SPC-5 have a different behavior, with respect to the sample rotation frequency, as compared with the $SR22_4^9$ sequence, as discussed below.

To obtain the plots with a y-axis in time units, each buildup curve corresponding to a particular sample rotation frequency was linearly interpolated to match buildup curves that were obtained at other sample spinning frequencies.

4.1.4.1. POST-C7. The first row in Figure 6 shows the simulated performance of the POST-C7 sequence, as a function of spinning speed, using the interaction parameters in Table 4. Figure 6a shows that the maximum excitation efficiency is achieved after ∼5 ms in the case of a −200 Hz dipole−dipole coupling constant and two CSAs of 50 ppm.

The excitation is severely degraded when the magnitude of the involved CSAs is increased to 100 ppm, as seen in Figure 6b.

4.1.4.2. SPC-5. The second row in Figure 6 shows the simulation results in the case of the SPC-5 sequence. The required rf field on the S-spins, $\omega_{\mathrm{rf}}^{S} = 5 \times (\omega_r/2\pi)$, is lower for SPC-5 than in the case of POST-C7. The SPC-5 sequence reaches the double-quantum excitation maximum at approximately the same time as that for the POST-C7 sequence, i.e., after ∼5 ms in the case of a −200 Hz coupling and CSAs of 50 ppm.

When the magnitude of the CSAs involved is increased to 100 ppm on each molecular site, the sequence performs poorly; however, a substantial improvement, compared to the POST-C7 sequence, is observed, at comparable rf fields.

4.1.4.3. $SR22_4^9$. The simulation results for $SR22_4^9$ are shown in the third row of Figure 6. We observe different features in the buildup curves when compared to previous sequences in that the excitation efficiency shows a nonlinear behavior, with respect to the sample rotation speed, ω_r. This nonlinear behavior of the excitation efficiency results in local maxima and minima, as a function of spinning speed as well as a function of the magnitude of the CSA tensors. The ϕ value used in the simulation was rounded to two decimal points, i.e., $\phi = 73.64°$.

We observe that, for a CSA of 50 ppm for each molecular site (Figure 6a), a local maximum is found at a spinning speed of $\simeq 9$ kHz and $\tau_{\mathrm{exc}} \simeq 4$ ms.

If the magnitude of the CSA is increased (Figure 6b), the maximum is found at a higher spinning speed and occurs at a somewhat shorter excitation time. In Figure 6b, the maximum occurs at $\omega_r/2\pi > 18$ kHz and in the τ_{exc} range of 2−6 ms. We also observe a prominent minimum at $\omega_r/2\pi \simeq 14$ kHz and $\tau_{\mathrm{exc}} \simeq 8$ ms. In terms of excitation efficiency, the $SR22_4^9$ sequence shows improved performance, compared to POST-C7 and SPC-5.

4.1.4.4. DRAWS. The last row in Figure 6 shows the simulation results for the DRAWS sequence. We observe in Figure 6a that, as in the case of POST-C7 and SPC-5, the maximum excitation efficiency of double-quantum coherence is building up to a constant value, as a function of the spinning speed. In Figure 6a, at a spinning frequency of $\simeq 6$ kHz, the maximum excitation efficiency remains constant ($>42\%$), even when the sample rotation frequency is increased. The theoretical maximum efficiency is 52% in the case of the DRAWS sequence.

As expected, the double-quantum excitation efficiency depends on the magnitude of the involved CSA. In the case of larger CSA, Figure 6b, a higher spinning speed ($\simeq 7.5$ kHz) is required to reach the optimum excitation efficiency. However, Figure 6a and b show that even with relatively large CSA, DRAWS is able to excite considerable amount of double-quantum coherence at moderate spinning speeds.

4.1.5. The Phase ϕ in the R Sequences. The unpredictable behavior observed in Figure 6 regarding the R sequences is attributed to the pulse-sequence-dependent parameter ϕ and the CSA interaction. In the case of small dipole−dipole couplings, which correspond to long excitation times and many RR′ elements, the profile of the resulting excitation curve is extremely sensitive to the exact numeric value of ϕ, as discussed in the literature.[43] Also, the excitation profile is similarly
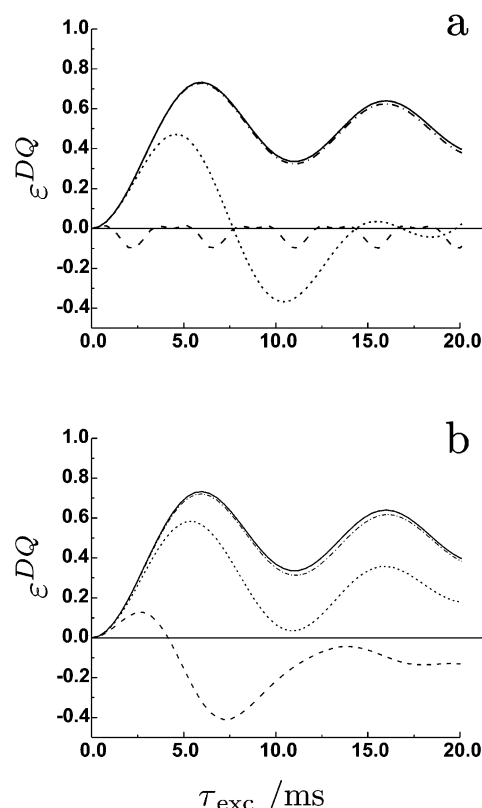
Figure 7. Figure showing the sensitivity on double-quantum buildup curves, with respect to changes in (a) the parameter ϕ and (b) the magnitude of involved CSAs for the sequence $SR22_4^9$. All curves were calculated using a dipole−dipole coupling constant of $b_{jk}/2\pi = -200$ Hz and isotropic shifts equal to 0 ppm. In panel a, the solid line was generated using the analytical expression of ϕ and a spin system with no CSA. The dash−dotted line was generated using $\phi = 73.64°$. The dotted line was obtained using $\phi = 73.6°$, and the dashed line was obtained using $\phi = 74°$. In panel b, all curves were generated using the analytical expression for ϕ, but the magnitude of the CSAs were varied. The solid line corresponds to a spin system with no CSA, and the dash−dotted line corresponds to a CSA of 25 ppm on each site. The dotted line corresponds to a CSA of 50 ppm on each site and the dashed line corresponds to 100 ppm on each site.

sensitive to the magnitude of the involved CSAs and, as simulations confirm, to a minor extent, the orientation of the involved CSAs. In Figure 7, this behavior is investigated by observing the shape of the double-quantum coherence buildup curve, when changing the exact numeric value of the parameter ϕ (Figure 7a) and when changing the magnitude of the involved CSAs (Figure 7b).

Figure 7a shows that the overall shape of the buildup curve is severely altered, as the precision of ϕ is changed. In Figure 7a, ϕ is changed from the analytical expression (solid line) to a number with no decimals (dashed line). We observe that, to match the analytical expression, the angle ϕ must be defined with a precision that is $>0.01°$. In practice, this can only be achieved using a phase shifter with a minimum resolution of 16 bits. Our home-built spectrometer has a 12-bit phase shifter, corresponding to a resolution in the rf phase of $0.09°$.

In Figure 7b, the magnitude of the involved CSA is changed, while the analytical expression of ϕ is used. We observe the same type of changes in the buildup curve as when the numeric precision of the parameter ϕ is changed. In Figure 7b, the solid line corresponds to no CSA, the dash−dotted line corresponds to 25 ppm on each site, the dotted line corresponds
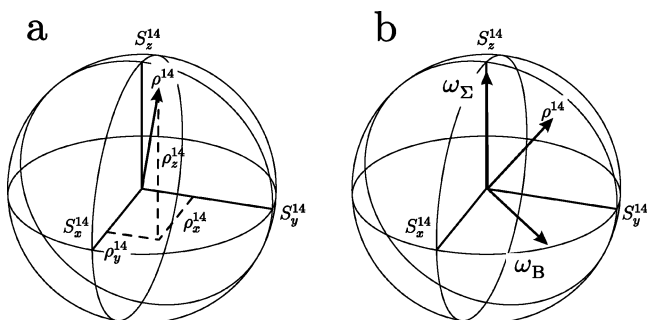
Figure 8. The double-quantum subspace. In panel a, the reduced density matrix, ρ^{14}, is shown with components S_z^{14}, S_x^{14}, and S_y^{14}. In the figure, S_x^{14} and S_y^{14} represent double-quantum coherence, whereas S_z^{14} represents longitudinal magnetization. The fictitious spin-1/2, ρ^{14}, interacts with two pseudo-fields, ω_Σ^{CS} and ω_B^{seq}, under application of a rf pulse sequence, as depicted in panel b. The pseudo-field ω_B^{seq} is solely a function of the applied rf pulse sequence.

to 50 ppm on each site, and the dashed line corresponds to 100 ppm on each site.

4.2. Spin Dynamics in the Double-Quantum Subspace. Although numerical simulations can reproduce experimentally observed trends, the spin dynamics underlying these trends is yet to be explained. In this section, we extend density-matrix calculations beyond the first-order limits used in the prior literature to describe the dynamics resulting from irradiation by an independent pulse sequence. These calculations are useful in understanding the dynamical basis for the relative efficiencies of γ-dependent and γ-independent pulse sequences.

In the following, the double-quantum dynamics is expressed in a three-dimensional subspace, S^{14}, spanned by the single transition operators S_z^{14}, S_x^{14}, S_y^{14},[61] which are defined as

$$S_z^{14} = \frac{1}{2}\{S_{jz} + S_{kz}\} \tag{15}$$

$$S_x^{14} = \frac{1}{2}\{S_j^+ S_k^+ + S_j^- S_k^-\} \tag{16}$$

$$S_y^{14} = \frac{i}{2}\{-S_j^+ S_k^+ + S_j^- S_k^-\} \tag{17}$$

and are monitored by the reduced density matrix, ρ^{14}. The components of ρ^{14} are obtained at time t as

$$\rho_z^{14}(t) = \text{Tr}\{S_z^{14}\rho(t)\} \tag{18}$$
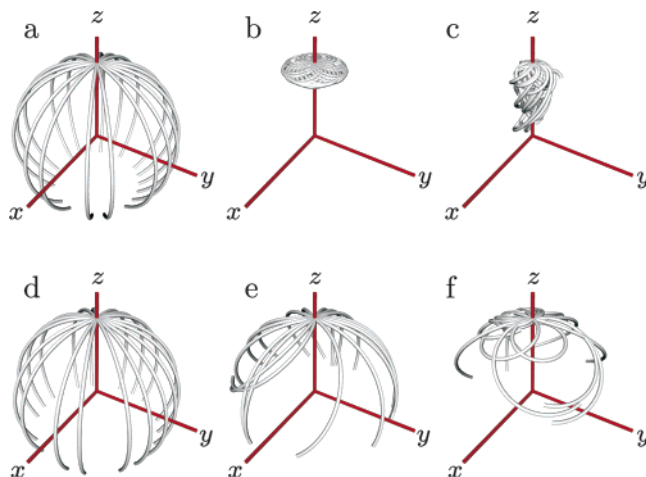
$$\rho_y^{14}(t) = \text{Tr}\{S_y^{14}\rho(t)\} \tag{19}$$

$$\rho_x^{14}(t) = \text{Tr}\{S_x^{14}\rho(t)\} \tag{20}$$

where $\rho(t)$ is the full spin density matrix (eq 11). The components of ρ^{14} (ρ_z^{14}, ρ_y^{14}, and ρ_x^{14}) are depicted in Figure 8a.

The reduced density matrix may be thought of as a fictitious spin-1/2 particle, evolving under a longitudinal pseudo-field $\omega_\Sigma^{CS}(\Omega, t)$ and a transverse pseudo-field $\omega_B^{seq}(\Omega)$, as depicted in Figure 8b. The longitudinal field ω_Σ^{CS} is dependent on both orientation and time and is given by

$$\omega_\Sigma^{CS}(\Omega, t) = \omega_j^{CS}(\Omega, t) + \omega_k^{CS}(\Omega, t) \tag{21}$$

where ω_j^{CS} and ω_k^{CS} can be found in ref 59.

(61) Ernst, R. R.; Bodenhausen, G.; Wokaun, A. *Principles of Nuclear Magnetic Resonance in One and Two Dimensions*; Clarendon Press: Oxford, U.K., 1987.

Figure 9. Trajectories in the double-quantum subspace, obtained for the sequences (a–c) C7 and (d–f) SPC-5. Each column represents different spin systems, exhibiting different magnitudes of the CSA. In each figure, the Euler angles α^{CR} and β^{CR} were held constant, and γ^{CR} was incremented from 0° to 360°, in steps of 30°. Spin interaction parameters were as follows. The dipole–dipole coupling constant, $b_{jk}/2\pi$, was equal to -200 Hz in all simulations. The spinning speed was 8 kHz. In panels a and d, the isotropic chemical shifts were 0 ppm. In panels b and e, each of the isotropic shifts was ± 50 ppm, and each of the anisotropic shifts was 50 ppm. In panels c and f, each of the isotropic shifts was ± 50 ppm and each of the anisotropic shifts was 150 ppm. A static magnetic field, B_0, corresponding to a ^{1}H nutation frequency of 400 MHz, was used in all figures.

The transverse pseudo-field is a function of the rf sequence that is applied on the spin system, as well as a function of crystallite orientation. The on resonant field may be written as

$$\omega_B(\Omega) = B(\Omega)e^{i\phi} \tag{22}$$

where B denotes the field amplitude and ϕ the phase. In the absence of chemical shifts, the fictitious spin ρ^{14} nutates about the pseudo-field ω_B. Maximum excitation of double-quantum coherence is obtained when ρ^{14} is rotated, from its initial position along the S_z^{14}-axis, down to the transverse plane, i.e., having a nutation angle of $\pi/2$. In a powder, and depending on the rf sequence that is being applied, different crystallite orientations lead to double-quantum dynamics occurring under pseudo-fields with different magnitudes and phases, as discussed below.

4.2.1. γ-Dependent and γ-Independent rf Sequences. In the following, we inspect the trajectories of the fictitious spin-1/2 ρ^{14}, as a function of different rf pulse sequences. Figure 9a–f show the trajectories of ρ^{14} for the sequences C7 (panels a–c) and SPC-5 (panels d–f). Each column corresponds to different magnitudes of the CSAs involved. In each figure, different trajectories correspond to different values of the Euler angle γ^{CR}, which was varied from 0° to 360°, in steps of 30°. In each figure, the Euler angles, α^{CR} and β^{CR}, were held constant. Each of the following figures were visualized and produced with the Gullringen program.

Figure 9a indicates that, for C7, although the magnitude of the effective pseudo-field B is the same for different γ^{CR} Euler angles, the phases are different, resulting in identical trajectories, with different phases about the S_z^{14}-axis. Figure 9a clearly shows that excitation of double-quantum coherence occurs independent of the molecular Euler angle γ^{CR}; i.e., the magnitude of the transverse component of ρ^{14} is the same, regardless of γ^{CR}. Figure 9b and c show ρ^{14} trajectories in the S^{14} space, obtained under larger CSAs. In Figure 9b, we observe that the
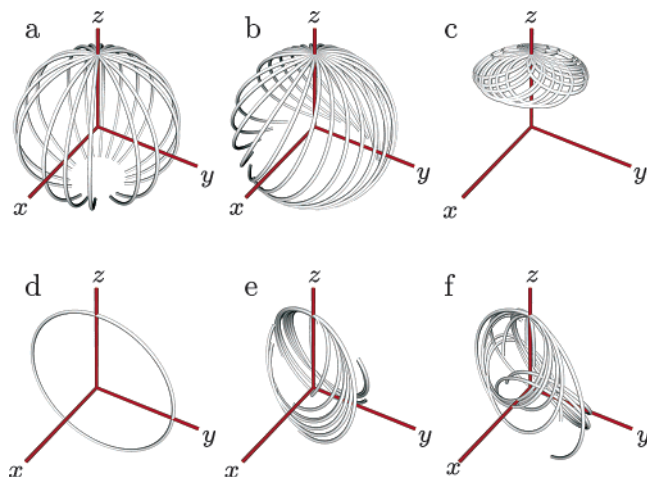
Figure 10. Fictitious spin-$^1/_2$ trajectories for (a–c) $SR22_4^9$ and (d–f) DRAWS. Spin interaction parameters were chosen as they were in Figure 9, except for the DRAWS sequence, where a spinning frequency of 4705 Hz was used.

evolution of the fictitious spin ρ^{14} now occurs under a severely tilted field, which is now close to the S_z^{14}-axis. The result is less-efficient excitation of double-quantum coherence. In Figure 9c, different γ values give different trajectories, indicating a breakdown of the sequence's independence of γ. This is expected, because the independence of γ is valid only to first order. As the CSA increases, higher-order terms become relevant and eventually dominate the spin dynamics. In the case of C7, terms in the interaction frame Hamiltonian resulting from incomplete CSA suppression result in coherence transfers out of the double-quantum space, S^{14}.

In Figure 9d–f, S^{14} space trajectories are shown for the rf pulse sequence SPC-5. In the absence of CSA (Figure 9d), the trajectories show that excitation of double-quantum coherence occurs independent of the Euler angle γ. For each single crystallite, the corresponding evolution of ρ^{14} occurs under an effective field that is perfectly aligned in the transverse plane.

Again, as the magnitude of the CSA increases, the evolution occurs under a tilted field and eventually (Figure 9f), even the independence of γ of the SPC-5 sequence breaks down. However, the failure of SPC-5 is not as severe as in the case of the C7 sequence, as expected from its superior performance in the preparation of double-quantum coherence under high CSA conditions.

Figure 10 shows similar trajectories for the $SR22_4^9$ (panels a–c) and the DRAWS (panels d–f) sequences. We observe that the $SR22_4^9$ sequence is much more robust than the C7 and the SPC-5 sequences, in regard to the suppression of large CSA terms. In Figure 10c, it seems that the independence of γ is still preserved (indicating good suppression of higher-order terms), whereas the excitation of double-quantum coherence is degrade, because of evolution under a tilted pseudo-field.

Figure 10d–f show trajectories obtained for the DRAWS sequence. The structure of these trajectories are different from the γ-independent sequences. The trajectories in Figure 10 are all in the same plane (y–z), indicating that the sequence gives rise to a pseudo-field that has the phase x or $\bar{x}$, regardless of the angle γ. However, inspection of the trajectories in Figure 10a, one by one, reveals that the magnitude of the pseudo-field is a function of the γ. This dependence on γ is seen more clearly

in Figure 10e, where, in the intermediate CSA limit, different trajectories show different S^{14} space nutation angles. As the CSA increases, the phase of the pseudo-field remain along the x-axis.

From the S^{14} space trajectories, DRAWS dynamics in the low CSA limit is described as nutation about fields with direction along the $+S_x^{14}$- or $-S_x^{14}$-axes, but with magnitudes that are dependent on γ. In the intermediate CSA limit, the effective fields develop components along the S_z^{14}-axis, presumably because of incomplete CSA suppression. This trend continues as the CSA increases, and, although the dynamics is complex, because of the dependence of these fields on γ, residual CSA effects never become as severe as those in the γ-encoded sequences. Therefore, as the CSA increases, the efficiency with which double-quantum coherence is prepared does not deteriorate for the DRAWS sequences as markedly as it does with the γ-independent sequences.

5. Discussion

Experiments and computer calculations probing the performance of several important recoupling sequences have been presented. Sequences studied were DRAWS, POST-C7, SPC-5, $R14_2^6$, $SR22_4^9$, and these sequences were performed using several molecular systems, exhibiting a fairly wide range of internuclear distances and chemical shifts.

The experiments confirm most of the features of each recoupling sequence already found in the literature. However, the aim of this study is to collect and place each sequence into perspective, relative to each other, regarding their overall performance on realistic molecular systems and under practical experimental conditions. In this sense, the study serves as an aid in the choice of a particular pulse sequence, depending on practical circumstances. Also, some new interesting features, not directly reported before in the literature, are observed, regarding the R-type of sequences, as discussed below.

In general, the excitation efficiency for any pulse sequence is dependent on the molecular system to which it is applied, as well as on experimental conditions, such as the sample rotation speed and the homogeneity of the applied rf fields. In the case of POST-C7, SPC-5, and DRAWS, the nature of the double-quantum coherence excitation efficiency, as a function of the CSAs involved and the spinning speed, is somewhat predictable. The efficiency for these sequences is generally degraded when the magnitude of the CSAs is increased while operating at a fixed spinning speed. A degraded efficiency, as a result of large CSAs, may, in the case of these sequences, be compensated by an increase in the sample rotation speed. It is important to note that this behavior is not observed in the case of the $R14_2^6$ and $SR22_4^9$ sequences. However, higher spinning speeds require stronger rf fields, and, depending on the overall performance of a particular sequence, the desirable spinning speed may not be practically achievable, because of probe limitations. Also, high rf fields may, in some cases, heat up and destroy the sample under study. This study demonstrates that, in the case of very large CSAs and small dipole–dipole couplings, DRAWS and $SR22_4^9$ are the only sequences that show a considerable amount of recoupling efficiency, acquired at practical, attainable rf fields.

In molecular systems with strong dipole–dipole couplings and moderate CSAs, the γ-independent sequences show superior performance, compared to the DRAWS sequence. In this type of molecular system, it is common to achieve double-quantum

efficiencies of 60%−70%, which is not theoretically possible with γ-dependent sequences, e.g., DRAWS.

As already mentioned, a striking feature of the R sequences is that they show nonlinear behavior in the recoupling efficiency, as a function of the sample rotation speed, the magnitude of the CSAs, and the mis-set of the parameter ϕ. This behavior results in local maxima and minima of the excitation efficiency. This behavior is generally undesirable, especially if the experiments are being performed on compounds where the magnitude of the CSAs are unknown.

In this paper, we have extended the description of double-quantum dynamics during dipolar recoupling beyond the first-order limit, which assumes large dipolar couplings and negligible CSA effects. To first order, double-quantum dynamics and the efficiency of double-quantum preparation are dominated by the dependence of the sequence on γ; therefore, a γ-dependent sequence such as DRAWS can never, as previously noted, achieve efficiency levels demonstrated by SPC-5, POST-C7, or the R sequences. However, given the trend toward using higher-field magnets in solid-state NMR, which will require dipolar recoupling in the presence of larger CSAs, the dynamics

of double-quantum preparation during recoupling may depart from the first-order theories that frequently appear in the current literature. The principal feature that limits double-quantum preparation efficiency appears to be the capability of these pulse sequences to suppress CSA effects. Ultimately, the performance of the present generation of dipolar recoupling pulse sequences remains largely dependent on the properties of the spin system, and the CSA, in particular. The dependence of the recoupling technique on γ is an important consideration only in the limit of negligible CSA and strong dipolar couplings. In the large CSA/weak coupling limit, the dependence on γ is of secondary importance, with regard to double-quantum coherence preparation. The experimental and theoretical double-quantum preparation efficiencies reported in this paper confirm this statement.

JA0294360